UNIVERSITAT DE BARCELONA

FACULTAT DE FÍSICA

Màster en Biofísica

Fluid Fronts in Hydrophilic and Hydrophobic Microchannels

Treball final del Màster en Biofísica 2008/09:
María Queralt Martín

Tutor: Aurora Hernández Machado

Contents

Abstract

An experimental setup is designed and experimental studies are done in order to investigate the behavior of fluid fronts in different microchannels. Different levels of hydrophobicity and pressure are explored, getting very different results for hydrophobic and hydrophilic microchannels [1]. For hydrophilic microchannels and any driving pressure difference the distribution of velocities corresponds to a Gaussian distribution and the front advances with $h \sim t^{\nu}$ with the classical Washburn exponent $\nu = 0.5$ for hydrophilic microchannels. The same results are obtained for hydrophobic microchannels at large driving pressure differences. For hydrophobic microchannels and when the pressure difference is decreased, the distribution of velocities corresponds to a Gumbel distribution that correctly characterizes rare events like avalanches and the front advances with an exponent ν as small as 0.38.

1   Introduction

In the last decade, the development of microfluidics has lead to the fabrication of micro fluid devices useful for chemical and biochemical analysis,

Figure 1: Chip built by Biosite Company for illness diagnosis, from [2]

biomolecular separation and micromixing to mention a few. Microfluidics aims to integrate many functions on a single device (lab-on-a-chip) for technological applications in physics, material sciences, biology and medicine [2, 3, 4, 5]. The so-called micro total analysis systems involve an extensive use of microfluidic systems for biological applications like cell culture, DNA separation, DNA sequencing and clinical diagnostic. This kind of devices pretend to perform a certain function, or several, with an unique integrated device. This allow to save space and, more important, to increase efficiency.

An example of this lab-on-a-chip devices for biological applications is found in a Biosite company chip [2], shown in figure 1, which analyses a droplet of blood in a microchannel and diagnose whether the patient had suffered a heart attack. It takes fifteen minutes to do the whole analysis, while traditional systems take several hours. Three proteins are detected whose secretion is higher when a heart attack has taken place.

A successful evolution of microfluidic devices is found in the production of pumps that can inject insulin to the liver for treatment of diabetes through a 500 μm diameter catheter. This means an important improvement from a medical point of view and also considering comfort for the patient. It has also been studying a further step in which pumps would be replaced by micropumps, having a whole integrated device which could be implanted inside humans body, as shown in figure 2.

Many examples like these can be found in literature [4, 5], realizing that interest for man-made microdevices has increased in recent years. Besides these kind of applications of microfluidic science, many microfluidic systems can be found in nature. For example, trees have a complex network of micro- and submicrometric sized capillaries that allows to supply water efficiently to the leaves.

Therefore, understanding the underlying physics in microfluidics is required to provide insight of the phenomena and achieve the possibility of designing new biological applications.

When a physical investigation of systems at micro scale is carried out,

Figure 2: Example of a micropump from Medtronic Inc. implanted in the body of a patient needing continuous injection of a product for illness treatment, from [2]

new phenomena are considered. In microfluidics, gravitational forces become negligible, and the equilibria that take their place are often instead dominated by surface forces such as capillarity, wetting and adhesion; the nature of the interaction between the fluid and the confining media determines largely the system response since the area-to-volume ratio is very large [7].

Mass transport in microfluidics is generally dominated by viscous dissipation, and inertial effects are generally negligible. The ratio of inertial to viscous forces on fluids is characterized by the so-called Reynolds number [8]

$$\text{Re} = \frac{\text{Inertia terms}}{\text{Viscous terms}} = \frac{v \cdot l}{\nu}, \tag{1}$$

where v is the characteristic velocity of the fluid, ν is its kinematic viscosity and l is the typical scale of the system.

For the case of microfluidics, it can be estimated using typical values of ν for water at room temperature ($\nu \sim 10^6 \ m^2/s$), the characteristic size of micro systems ($l \sim 100 \ \mu m$) and typical velocities achieved ($10 \ \mu m/s$), having $\text{Re} \sim 10^{-3}$. This low value of Re affirm that viscous forces typically overwhelm inertial forces, and the resulting flows are linear.

The ratio of diffusion to convection in microfluidics is also very small, having that mixing occurs by diffusion alone, which results in longer mixing times than in macroscopic systems.
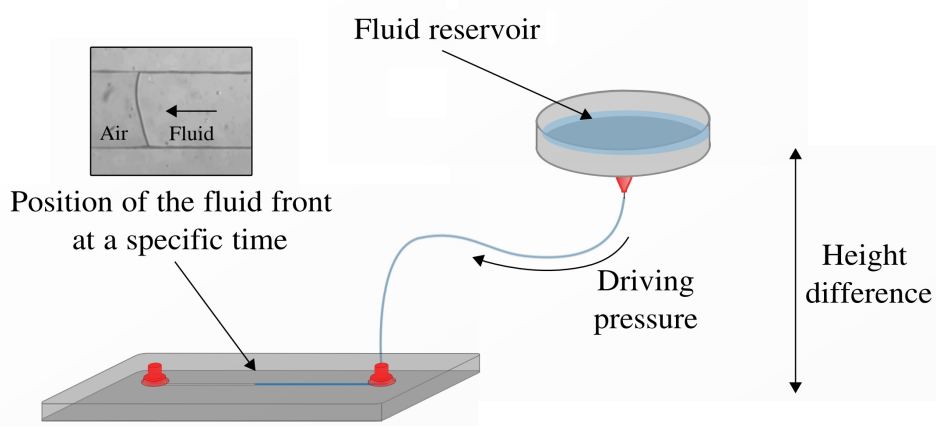
3

Figure 3: Scheme of the experiments carried out in this work. Dynamical behavior of the position of the fluid front for different constant driving pressure differences is studied. Pressure differences are obtained through height differences between the fluid reservoir and the microchannel

Therefore, new phenomena become important when considering microfluidics. Behavior of fluids in small channels needs a deeper study to understand this new phenomena.

In this work the advancement of fluids inside a microchannel due to a pressure gradient is studied (see figure 3). The dynamics of a liquid meniscus when it is driven into a microchannel at constant driving pressure differences is analyzed, studying the spatially averaged position $h(t)$ and its mean velocity $v(t)$. The aim is to see how the driving pressure and the wetting conditions of the channel may affect the time evolution of the interface. It is studied using microchannels with different levels of hydrophobicity and different roughness. Although typical biological fluids, like blood, are viscoelastic, in this work Newton fluids (water) are used. This has to be taken as a first step to characterize dynamics of biological fluids.

The level of hydrophobicity is controlled selecting specific types of materials for microchannel fabrication. The roughness is the intrinsic of the walls of the microchannel; it is actually not controlled during the manufacturing of the channel, but it is assumed to be important enough to affect the dynamics of the fluid front.

2   Theoretical Basis

To explain the behavior of a fluid in a microchannel, fluid mechanics equations have to be studied.

In the case of this work, only the macroscopic analysis of equations will be solved in order to show what are the established results in the dynamics

4

Figure 4: Scheme of a Hele Shaw geometry. The front of fluid advances between two infinite plates separated a small distance b

of the front position at constant driving pressure in macroscopic channels. For microchannels, the study will be carried out experimentally.

To start with the theoretical analysis, the most general equation in fluid mechanics, the so-called Navier-Stokes equation, has to be solved:

$$\rho \left(\frac{\partial \vec{v}}{\partial t} + \vec{v} \cdot \vec{\nabla} \vec{v} \right) = -\vec{\nabla} p - \vec{\nabla} \cdot \vec{\vec{\tau}} + \vec{f} \, , \tag{2}$$

where ρ is the fluid density, $\vec{v}$ is the velocity of the fluid, p is the pressure, $\vec{\vec{\tau}}$ is the strain tensor and $\vec{f}$ is the external force.

This equation arises from the second law of Newton for continue systems and incompressible fluids.

To apply equation 2 to the system considered, the geometry has to be defined. Since the analysis made is supposed to be a starting point of a microscopic analysis, it is interesting to choose a geometry alike to the one in microchannels. Since several microchannels used have rectangular section, Hele Shaw geometry is considered the most convenient. This geometry consists in two infinite and parallel plates separated by a small distance, as shown in figure 4.

In this geometry, it is assumed that the front advances in y direction, having:

$$\vec{v} = (0, v_y, 0)$$

Velocity modulus will not depend on x and y directions because it is assumed that top and bottom plates are infinite. Therefore, velocity will be:

$$\vec{v} = v_y(z) \; \vec{a}_y$$

For Newton fluids the stress tensor is directly proportional to velocity gradient, $\vec{\vec{\tau}} = -\eta \vec{\nabla} \vec{v}$, where η is the viscosity of the fluid, having:

$$\rho \left(\frac{\partial \vec{v}}{\partial t} + \vec{v} \cdot \vec{\nabla} \vec{v} \right) = -\vec{\nabla} p + \eta \nabla^2 \vec{v} + \vec{f} \tag{3}$$

Since Re number is small, equation 3 turns into the so-called Stokes equation, where inertia terms and time dependence do not play any role in the behavior of the system:

$$\eta \vec{\nabla}^2 \vec{v} = \vec{\nabla} p - \vec{f} , \tag{4}$$

The only external force present in the system is the pressure gradient applied, so $\vec{f}$ can be eliminated from equation 4.

The pressure gradient used is the same than in the experiments. It is caused by a difference in height between the microchannel and the fluid reservoir, that will drive the fluid into the microchannel. That means that pressure gradient will only depend on y direction. Therefore, the equation to be solved is:

$$\frac{d^2 v}{dz^2} = \frac{1}{\eta} \frac{dp}{dy} \tag{5}$$

This differential equation has the trivial solution:

$$v(z) = \frac{1}{2\eta} \frac{dp}{dy} z^2 + Az + B , \tag{6}$$

where A and B are constants to determine.

Boundary conditions need to be defined to determine the constants above. These boundary conditions will refer to the velocity at the plates and are taken as follows:

$$v(z = 0) = v(z = b) = 0 \tag{7}$$

Using them, unknown constants from equation 6 can be determined, getting:

$$v(z) = \frac{1}{2\eta} \frac{dp}{dy} z(z - b) \tag{8}$$

Now the average is calculated to eliminate the dependence is z direction and obtain an spatially averaged velocity:

$$< v >= \frac{1}{b} \int_0^b v(z) \, dz = -\frac{b^2}{12\eta} \frac{dp}{dy} \tag{9}$$

Equation 9 is known as classic Darcy law. It can be seen that mean velocity depends on fluid and system properties, which have constant values, and also on pressure gradient, which may depend on front position.

Pressure gradient is introduced in the experiment as a constant difference in height between the microchannel and the reservoir of fluid. Because of that, the gradient can be approximated to a finite difference, having:

$$\frac{dp}{dy} \simeq \frac{\Delta p}{h} \ , \tag{10}$$

where h is the position of the front of fluid and $\Delta p = \frac{p_i - p_{ap}}{h}$ is the driving pressure difference, with p_i as the pressure at the interface position and p_{ap} as the applied pressure. Both pressures are assumed to be constant, having a constant pressure gradient.

Therefore, Darcy law from equation 9 has the form:

$$< v >= -\frac{b^2}{12\eta}\frac{\Delta p}{h} \tag{11}$$

From this equation the dynamics of the averaged position h of the fluid front is analyzed, having:

$$< v >= \frac{dh}{dt} = -\frac{b^2}{2\eta}\frac{\Delta p}{h} \ ; \qquad \frac{dh}{dt} = -\frac{b^2\Delta p}{12\eta}\frac{1}{h} \qquad \Rightarrow$$

$$\Rightarrow \qquad h \sim t^{1/2} \tag{12}$$

This result is the so-called Washburn law. It states that dynamics of the front of a fluid follows a power law $h \sim t^\nu$ with $\nu = 0.5$ when a macroscopic Hele-Shaw geometry is considered.

For the case of the dynamics of the fluid in microchannels, theoretical studies have been carried out studying the dynamics of front position in hydrophilic and hydrophobic microchannels [9]. For the case of hydrophilic microchannels, it is found that the dynamics of front position follows the typical Washburn law $h \sim t^{1/2}$. In hydrophobic microchannels, the dynamics of front position follows a power law $h \sim t^\nu$, obtaining a non-classical exponent ν as small as 0.4.

In this work, the dynamics of the fluid front for microchannels will be studied experimentally, obtaining a power law $h \sim t^\nu$ with an exponent $\nu = 0.5$ for hydrophilic microchannels and a $\nu = 0.38$ for hydrophobic microchannels, in good agreement with these theoretical results.

3   Experimental Setup

The aim of this work is study the dynamics of a front of water driven into a microchannel through a constant pressure difference. In figure 5 is presented a photograph of the setup.

In the experiment there are two key elements: fluid and microchannels. The fluid chosen is purified water, which is a Newton fluid. In some cases, water will be mixed with ink in order to get better images. This ink is

Figure 5: Photograph of the experimental setup

carefully filtered and mixed in enough small concentrations to not affect fluid behavior.

Microchannels are important because their size and composition will determine the dynamics of the front. In this work, two kind of materials have been used: PMMA, which is more hydrophilic, and PDMS, which is more hydrophobic. The microchannels used also have different sizes, going from 500 μm to 100 μm width. These differences are mainly due to fabrication techniques used.

3.1 Microchannels

Microchannels are one of the key elements in the experiment because they allow to explore different wetting and roughness conditions. Wetting conditions are controlled selecting specific types of materials for microchannel fabrication. Two types of materials are used. One is hydrophilic (PMMA) and the other is hydrophobic (PDMS).

Both types of microchannels have an intrinsic roughness which is not controlled during their fabrication, but it is assumed to be important enough to affect dynamics of the fluid front.

In figure 6 these microchannels are shown. They have different sizes and different forms because of the different fabrications, but all of theme belong to the micrometer scale, allowing the study of the properties of interest in this work.

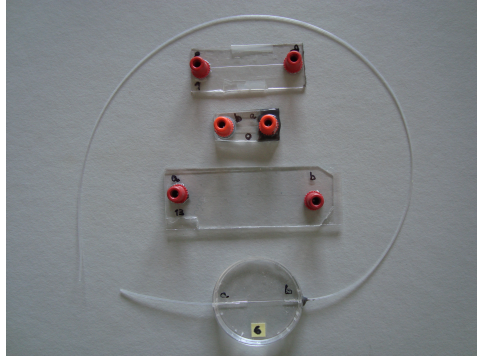In table 1 sizes and material of each type of microchannel used in the

Figure 6: Different types of microchannels used in the experiments. From top to bottom, they correspond to types 1, 2, 3 and 4 from table 1

Type	Material	Section Shape	Sizes	Total Volum
1	PMMA	Cylindrical	150 μm diameter, 3.2 cm long	0.57 μL
2	PDMS	Rectangular	387 μm width, 70 μm height, 1 cm long	0.27 μL
3	PDMS	Rectangular	100 μm width, 7 μm height, 6 cm long	0.04 μL
4	PDMS	Cylindrical	150 μm diameter, 1.6 cm long	0.28 μL

Table 1: Types of microchannels used in the work

experiments are shown .

3.2   Experiment Design

The mean characteristic of the experiments carried out in this work is the constant pressure difference set for driving the fluid front inside the microchannels. The experimental setup is characterized in such a way this requirement is satisfied. In figure 7 is shown a diagram of the setup.

The setup has a plate where the reservoir of water is contained, which is connected to the microchannel through a needle and a thin tube. Water plate has been built with a plastic petri dish and a hole has been made to glue the needle.

The plate is held in a platform with free movement in vertical direction, to allow changes in height and, therefore, changes in pressure. When the experiment is prepared, height is determined and fixed until the end of the experiment. Because of the procedure, the choice of good heights, that is, good pressures, is made in a trial and error method.

There is no way of determining the exact pressure induced in each experiment because of the simplicity of the setup, but an estimation of it can be made knowing height difference between microchannel and water plate
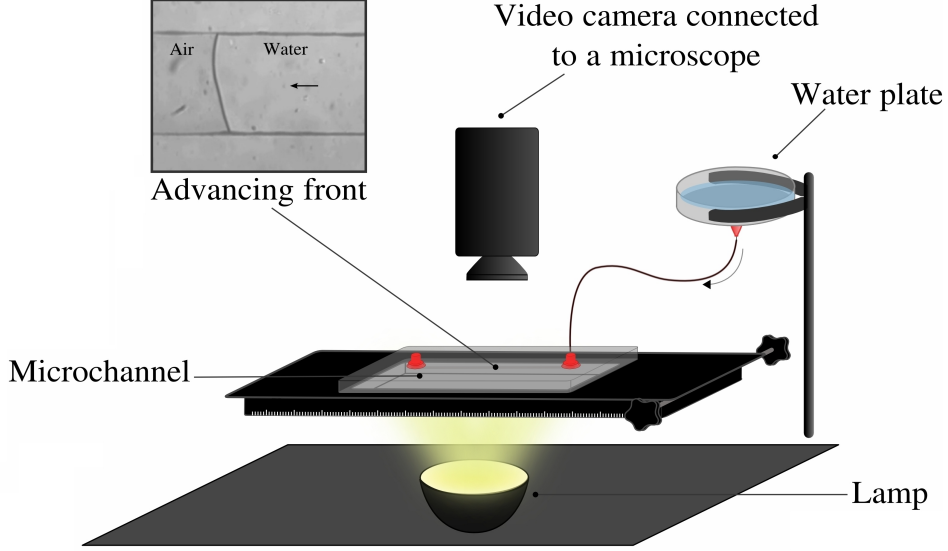
9

Figure 7: Experimental setup for measurements at constant pressure

with a specific water quantity.

In figure 8, it is shown how this estimation is calculated. If the fluid is in equilibrium, pressure at one side of the microchannel will be equal to pressure at the other side, having:

$$p_{atm} + p_{front} = p_{atm} + \rho g \Delta h \qquad \Rightarrow \qquad p_{front} = \rho g \Delta h \ , \qquad (13)$$

where $\rho g \Delta h$ is pressure of fluid due to the presence of gravity.

Therefore, Δh will be the cause of the difference in pressure that will push water front. Despite figure 8, where the plate is much above the chip, in real experiments plate and microchannel are almost at the same level, having a typical difference between them of 10 mm. Then:

$$\left. \begin{array}{l} \rho = 10^3 \ kg/m^3 \\ g = 9.8 \ m/s^2 \\ \Delta h = 10 \ mm \end{array} \right\} \Rightarrow p_{front} = \rho g \Delta h = 98.1 Pa \sim 10^2 Pa \qquad (14)$$

Therefore, the driving pressure differences applied in the experiment are of the order of 100 Pascals.

The choice of a flat dish to contain the fluid is due to the necessity of having a flat container where water is placed and, because of the constant pressure condition, water level is constant during all the experiment. Because of that, petri dish diameter has also been chosen in such a way water level variation due to front advancing is negligible.
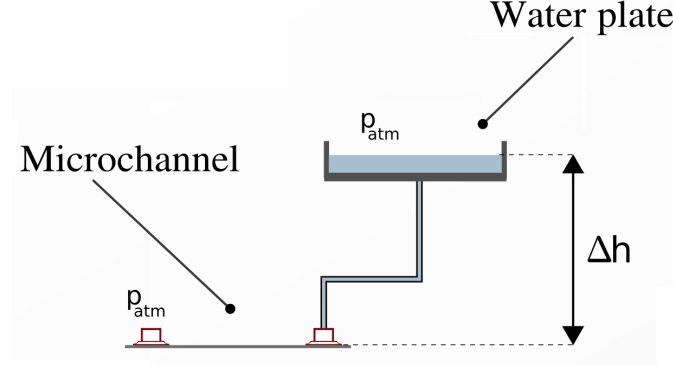
Figure 8: Pressure estimation from difference in height between water level and microchannel

To be sure that water level remains stable during the experiments, a estimation of how water level changes when a microchannel is filled is calculated. First, it is calculated an estimation of the volume of water held in the microchannel when an experiment is ended (see figure 9). To do it, the bigger microchannel is used; it is a cylindrical one, with 150 μm diameter and 3.2 cm length, having a volume of 0.6 μL.

This volume will cause water level variation in the plate. This plate, as shown in figure 9, is cylindrical with a diameter $\Phi = 9.0$ cm, having an area of 6361.7 mm^2.

Then, the volume of water extracted from water plate to fill the microchannel will produce a height variation of 0.1 μm.

This height variation is translated into a pressure variation, having:

$$\Delta p = \rho g \ \Delta H \simeq 9.8 \times 10^{-4} Pa \sim 10^{-3} Pa \tag{15}$$

This quantity can be compared with pressure exerted in the experiments, calculated in equation 14. It can be seen that the difference is of five orders of magnitude, a difference large enough to be negligible.

The microchannel is supported in a platform with long travel track. The horizontal movement of the microchannel is necessary because it is too much long to appear entirely in the screen. Movement of the track is performed thanks to a screw that allows a soft movement, which is extremely necessary in order to avoid perturbations in the system during the experiment.

Camera provides analog videos, which are converted to digital data and saved in a computer through a digital converter card. Videos are saved in the computer and then images are extracted with a special program. Images, after recordering and extraction, have a size of 720 x 576 pixels.
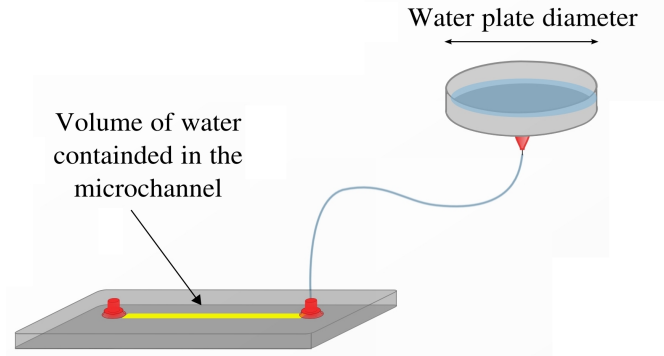
Figure 9: Scheme of water contained in a microchannel when an experiment is ended

All the setup is put on an antivibration table in order to avoid perturbations.

It is important to point out that the setup, although being very simple, satisfies the mean requirements to guarantee good measures of the system; that is, constant pressure during the experiment, isolation and providing good images.

3.3 Image Analysis

When video is captured, images are extracted and analyzed with a program written in MATLAB®. This program analyzes all the images from the video, allowing to have very good statistics. Depending on microchannel used, image changes because they have different sizes and forms. In figure 10 some of these images are shown to allow the reader to have an idea of what kind of image has to be analyzed.

The program written in MATLAB® allows to analyze images of all this different microchannels. First, the program takes an image and cuts it, keeping only the area where the microchannel is. Then, it converts it into a binary one, converting into white the pixels with a gray value below a threshold and into black the ones with the value above the threshold ; after, it cleans the resulting image, removing spots due to material defects and light shadows. In appendix B is shown the code of this program.

After this process, a good binary image is obtained, allowing the program to recognize where the interface is. The threshold is a parameter that can be changed, which allows to analyze such different images shown in figure 10. In figure 11 is shown an example of the steps explained.

Before starting constant pressure experiments, the program was checked analyzing some videos made with constant velocity, using a syringe pump. The dynamics obtained experimentally where compared with the expected behavior, that is, a constant velocity, finding very good agreement. In figure
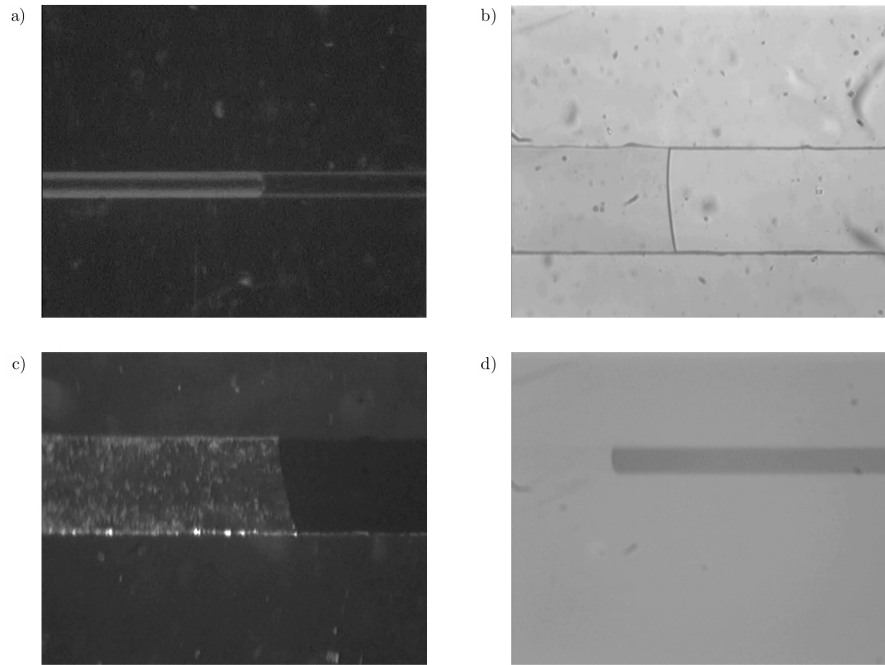
Figure 10: Images of several microchannels. In (a) and (b) are shown PMMA and PDMS microchannels receptively, with water. In (c) and (d) are shown two different PDMS microchannels filled with a mix of water and ink. In all images fluid goes from right to left
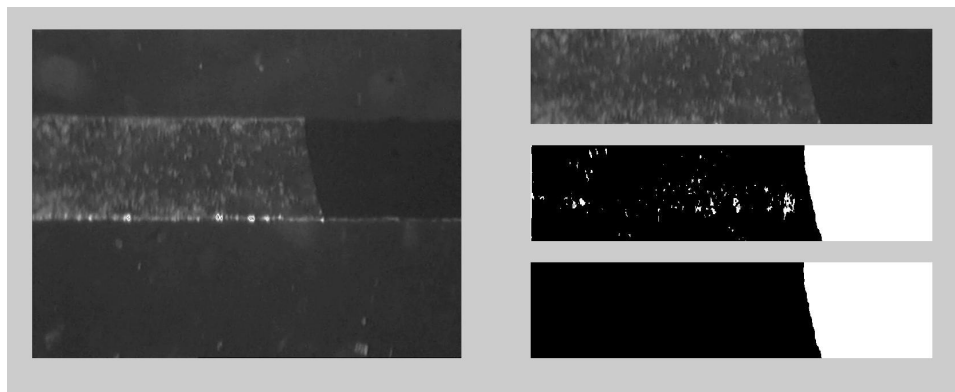

Figure 11: Steps for image analysis. At the left, original image is shown. At the right, from up to down the following images are shown: the cut one, the dirty binary image and finally the cleaned image used for position determination
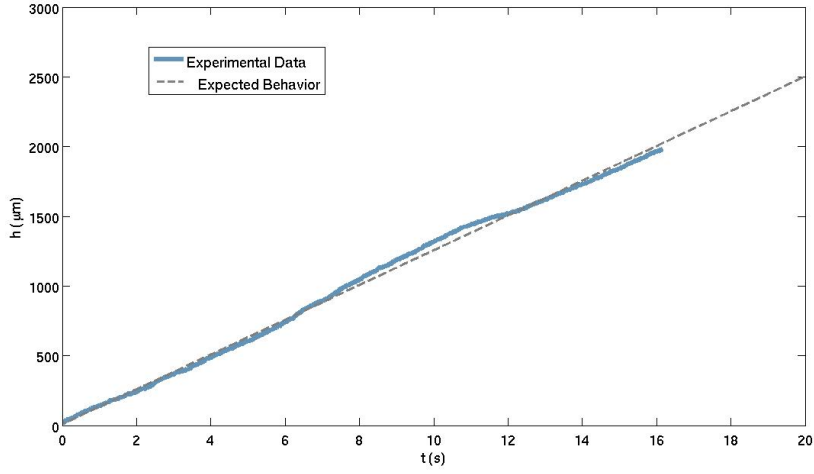
13

Figure 12: Experimental data of the dynamics of the front position (solid line) when a pump is used to provide constant velocity. The agreement with the expected behavior (dashed line) allows to check that the programs created for analysis of images work well

12 is shown the result of one of these tests.

Oscillations observed in the experimental behavior of figure 12 appear because the pump does not push water in an exactly constant way. Therefore, it can be seen that there is a very good agreement between the experimental results obtained with the MATLAB® program and the expected behavior, concluding that the program works well.

Therefore, it has been written a simple program that allows to analyze automatically all images from the experiment.

3.4 Data Treatment

When images are analyzed, a file with space values is obtained. This data is measured in pixels and, to translate it into a real space magnitude, that is, into micrometers, relation between pixels and micrometers has to be calculated. To obtain this relation, it is necessary to measure the value in pixels of an object which size is well known. For this purpose, a tungsten wire was selected. This material has an exact width of 50 μm, specially fabricated for applications in which is necessary to have a controlled width. To know its correspondence in pixels, it was put in the microscope and recorded with the same process than in an experimental video.

Finally, relation obtained was:

$$\text{Relation} = 6.25 \ \mu\text{m/pixel} \tag{16}$$

This means that spacial resolution of videos is of this size.

On the other hand, obtaining time data is trivial because it is known which time corresponds to each image. Typically it is extracted an image each second of the video, having a time resolution of 1 second. This is enough because interface runs so slowly that resolution in time is determined by resolution in space.

Finally, data of time and front position are obtained from the experiments. The experiments have intrinsic errors that will affect all measures and results. It is important to calculate them to know how believable are results shown.

Time has not any error associated because is a magnitude directly determined from the recordering, but front position actually does. The analysis programs determine front position with only the error of the resolution of the system, that is, a pixel. This value, translated to real distance using relation 16, corresponds to 6.25 μm. Therefore, this is the error of direct data values:

$$\delta h_i = 6.25 \ \mu m \tag{17}$$

But these are not the data used for result analysis because mean position of the front is calculated. That is, when a microchannel is recordered, it has a specific width, which is translated in a width of several pixels (here called rows), in which each of them will have a front position associated (see figure 11). Then, to obtain a unique value for the front position at each value of the time, the mean h has to be calculated. This will also reduce the error associated to the measure, having:

$$h(t) = \frac{1}{N} \sum_i h_i(t) \ , \tag{18}$$

where N is the number of rows (that is, the width of the microchannel in pixels) and $h_i(t)$ is front position of each of this rows at time t, and:

$$\delta h = \frac{\delta h_i}{\sqrt{N}} \ , \tag{19}$$

where δh_i is the same for all rows because is the error from equation 17. In order to obtain a final value for this expression, number of rows has to be set. It depends on microchannel width and image quality (if, for example, there were shadows in the walls of the microchannel, rows would be reduced); therefore, it will change with the experiments. But here the smallest number of rows possible is chosen in order to get an upper limit of the error, and this number is 30 rows.

Therefore, the error will be:

$$\delta h = 1.14 \ \mu m \tag{20}$$

To realize if this number is large or small, it is calculated the relative error, where total width of the microchannel is introduced. Once again, in order to obtain the upper limit, the smallest microchannel width is used, that is, type 3 value from table 1: $w = 100 \ \mu$m width. Then:

$$\delta h_{relative} = \frac{\delta h}{w} \times 100 \simeq 1 \ \% \tag{21}$$

Thanks to this result, it can be concluded that once mean front position is determined, values are good enough to give reliable results.

Once the time t and the averaged front position h are calculated, they are plotted in linear and logarithmic scales to observe its relation $h(t)$.

The next step in the analysis of data consists in calculate the numerical derivative of the averaged front position, that is, numerical averaged velocity. This is directly calculated using the relation:

$$v_j = \frac{h_{j+1} - h_j}{t_{j+1} - t_j} \equiv \frac{h_{j+1} - h_j}{\Delta t} \ , \tag{22}$$

where j is the index referred to the time.

The corresponding error will be:

$$\delta v_j = \sqrt{2} \ \frac{\delta h_j}{\Delta t} = \frac{1.61}{\Delta t} \ , \tag{23}$$

where δh_j is the value of equation 20. Therefore, it can be seen that the error will decrease when Δt (also called time step) is increased. This occurs because the resolution in the space will determine the resolution in the time. That is, the time step has to be set is such a way the front position would have time enough to advance a distance detectable experimentally. Therefore which time step is needed depends on the velocity of the front position, which changes for each realization.

Because of that, when velocity data is obtained for each experiment, it is made a study of which time step is needed for obtaining a velocity with small error for use in further calculations. An example of this is shown in figure 13. It can be observed that the first plot is very noisy, the second one a little less noisy and the last one is much better, revealing the real behavior of velocity. The unique difference between these plots is the time step used in velocity calculation.

Once velocity data is obtained, its distribution function is calculated. To do it, a program for MATLAB® is written, where data is normalized, as
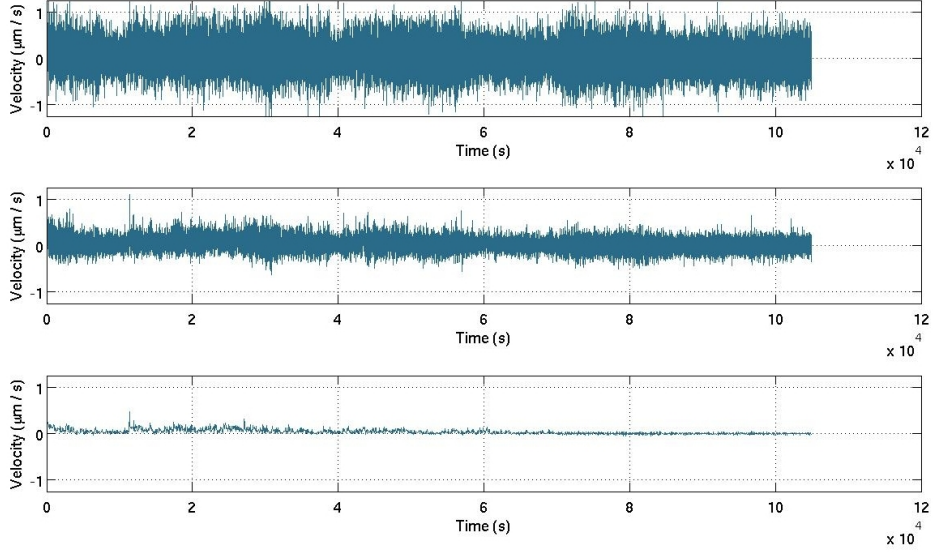
Figure 13: The same velocity data set is plotted versus time for three different time steps: first with $\Delta t = 1$, when all data is used. The second when Δt is a little bigger and the last one when Δt is big enough for having good data. It can be observed how data improves drastically only changing time step

seen in appendix B.

Finally, the power spectrum of averaged velocity is calculated. The power spectrum P of a function f corresponds to the expression

$$P(\omega) = \left[\mathrm{abs} \left(\int_0^\infty f(t) \, \mathrm{e}^{-i\omega t} dt \right) \right]^2 , \qquad (24)$$

where ω is the frequency corresponding to each time t. The power spectrum itself is the Fourier transform of the auto-correlation function, having

$$R(t) = \frac{1}{2\pi} \int_0^\infty P(\omega) \, e^{i\omega t} d\omega. \qquad (25)$$

The auto-correlation function represents the relationship of long and short-term correlation within the signal itself. That is, a high value in the low spectral region means a high correlation in a very long time scale and a high value in the high region of the spectrum implies high correlations in short time scales. Therefore, power spectrum will allow to explore the time correlation of the averaged velocity in the experiments.

17

For the calculation of the power spectrum of the numerical velocity of the experiments, the Fast Fourier Transform algorithm [11] is used. It is calculated using MATLAB®. Source code is showed in appendix B.

4 Results

The results obtained in this work can be divided in two main parts: the first one with results from hydrophilic microchannels and the second one with the ones from hydrophobic chips. The experiments are the same for both types of microchannels, but results are different.

4.1 Results for hydrophilic microchannels

To start, PMMA hydrophilic microchannels are used. Height of the setup is changed in different realizations in order to obtain a different pressure for each one. For the first realization, a specific height is chosen and it is lowed in the next experiments. For each one, images are analyzed and global position of the front as a function of time is obtained. These results are shown in figures 14, 15, and 16.
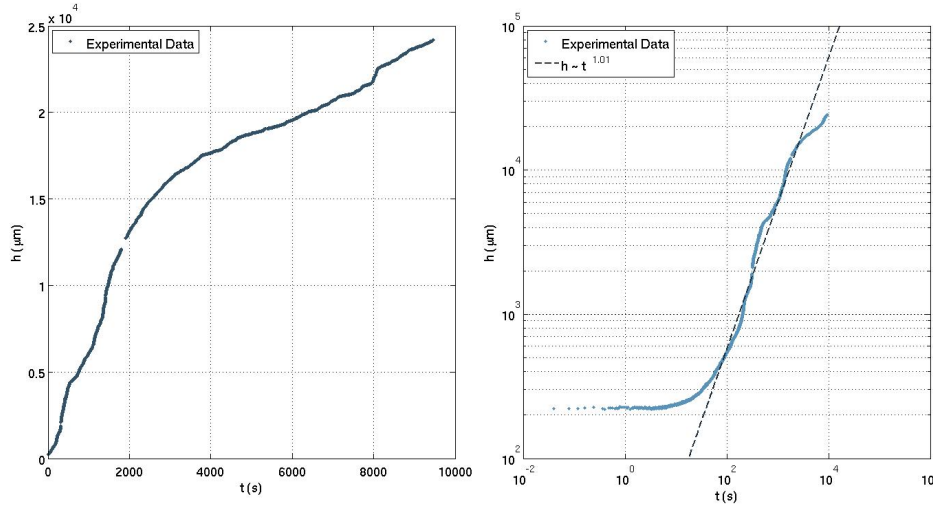

Figure 14: Experimental dynamics of the averaged front position in a hydrophilic microchannel for high driving pressure differences. It is shown in a linear scale (at the left) and a logarithmic scale (at the right)

They are plotted in a linear and logarithmic scale to study the dependence of the front position with time. It can be observed that they follow a power law:
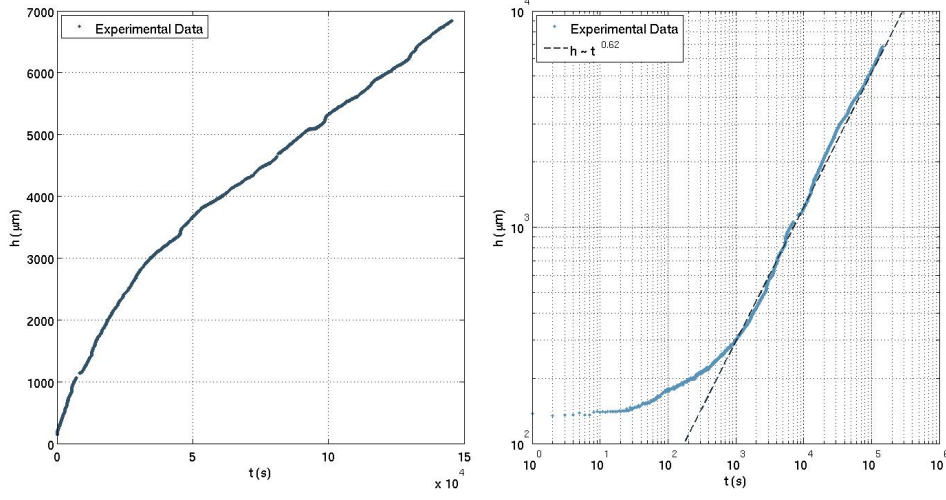
$$h \sim t^{\nu}. \tag{26}$$

18

Figure 15: Experimental dynamics of the averaged front position in a hydrophilic microchannel for medium driving pressure differences. It is shown in a linear scale (at the left) and a logarithmic scale (at the right)
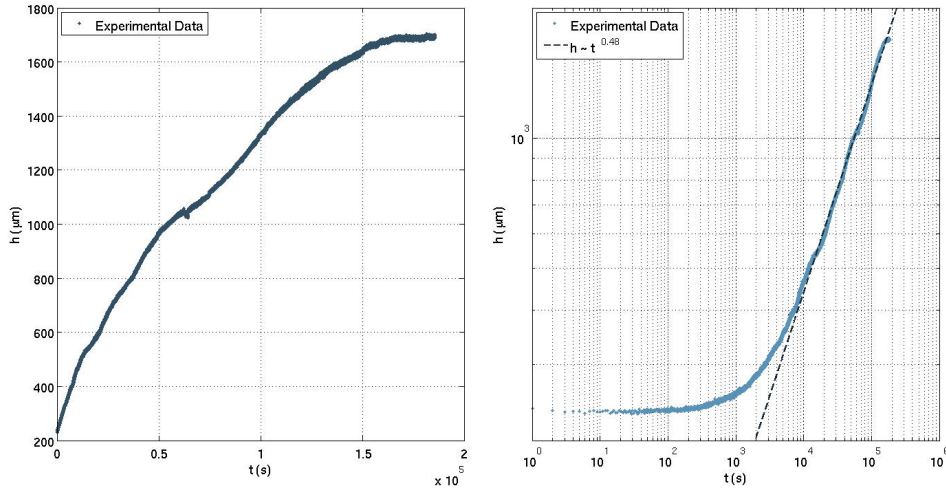

Figure 16: Experimental dynamics of the averaged front position in a hydrophilic microchannel for low driving pressure differences. It is shown in a linear scale (at the left) and a logarithmic scale (at the right)

The exponent ν changes as the driving pressure applied is different. When pressure is high, the dependence is $\nu = 1$, which means that velocity is constant; as pressure is lowed, the exponent in time dependence starts to be smaller, taking a smallest value when pressure is very low, hav-
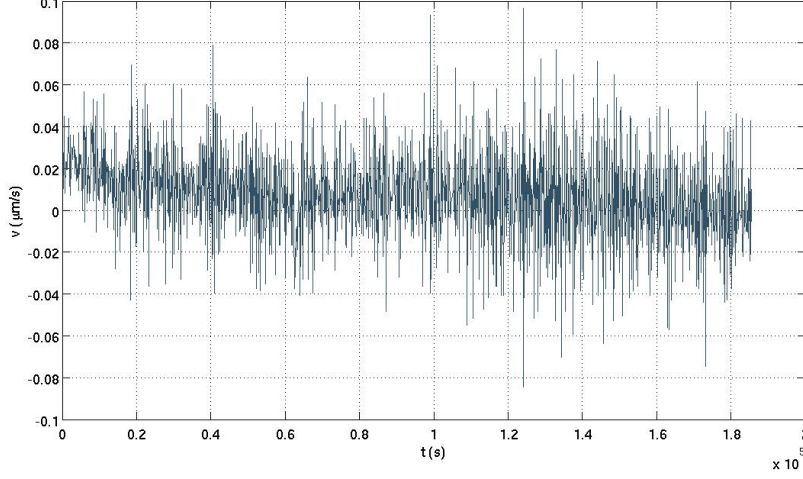
19

Figure 17: Experimental velocity as a function of time of a fluid front advancing in a hydrophilic microchannel

ing $\nu = 0.5$, which agrees with the Washburn law. This exponent value is the smallest obtained, despite very low pressures have been applied. It has sense that exponent gets larger when pressure increases because then walls effect is lost due to the high velocity of the front.

It has to be noticed that in figures of front position versus time in logarithmic scales, there is at the beginning a transitory regime. The existence of this regime (and sometimes another similar at the end of the video) is due to the influence of connections in the microchannel. Because of that, flow takes some time to stabilize and behave following the exponent calculated.

Now the averaged velocity is calculated. It is showed in figure 17.
It can be observed that it presents many fluctuations, having

$$v(t) = v_o(t) + \delta v(t), \tag{27}$$

where $v_o(t) \sim t^{\nu-1}$ is the mean temporal dependency that comes from equation 26. The fluctuating term $\delta v(t)$ is attributed to the pinning effects at the interface induced by the roughness present at the surfaces of the channel. The point is to study how these fluctuations behave when the applied pressure is modified. In order to characterize these fluctuations, their distribution is calculated. The same kind of distribution is obtained for the realizations carried out at different driving pressures. An example of these distributions is shown in figure 18. It can be observed that the distribution
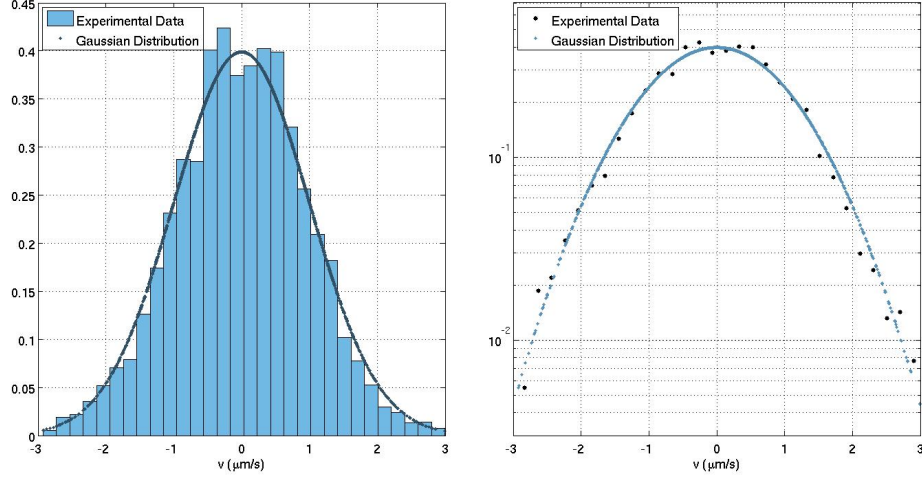
20

Figure 18: Distribution of the experimental fluctuations of the velocity of the fluid front in a hydrophilic microchannel and a Gaussian distribution, in linear and semilogarithmic scales

is very symmetric, having that velocity fluctuations are basically Gaussian

$$F(x) = \frac{1}{2\pi} \exp(-\frac{1}{2}x^2), \quad \text{with} \quad x = \frac{v - v_0}{\sigma_v}. \tag{28}$$

From velocity profile, it can also be calculated the power spectrum, as shown in figure 19.

It is observed that the values of the power spectrum are randomly distributed, as expected when the distribution of data is Gaussian.

4.2   Results for hydrophobic microchannels

In this case, PMMA microchannels are replaced by PDMS ones to obtain hydrophobic conditions. Purified water is used and height is changed in order to have realizations at different constant pressure values. Height is chosen to have an experiment at high pressure and then it is lowed in different realizations. In figures 20, 21 and 22 the dynamics of the front position for several of these realizations is shown: one for high pressure realization, other for medium pressure and a last one for very low pressure.

It can be observed that the dynamics of front position follows a power law:

$$h \sim t^\nu \tag{29}$$

This dependence is also found in the dynamics of front position for hydrophilic microchannels, but for hydrophobic microchannels the values ob-
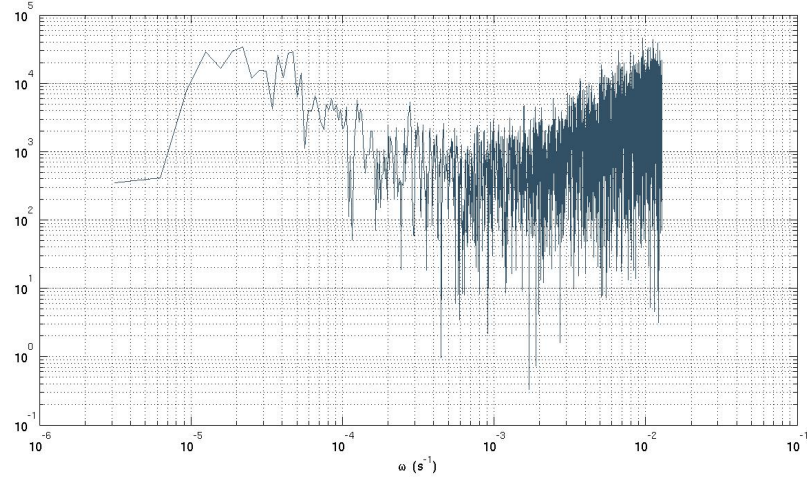
21

Figure 19: Logarithmic representation of the power spectrum of the experimental velocity of a fluid front in a hydrophilic microchannel
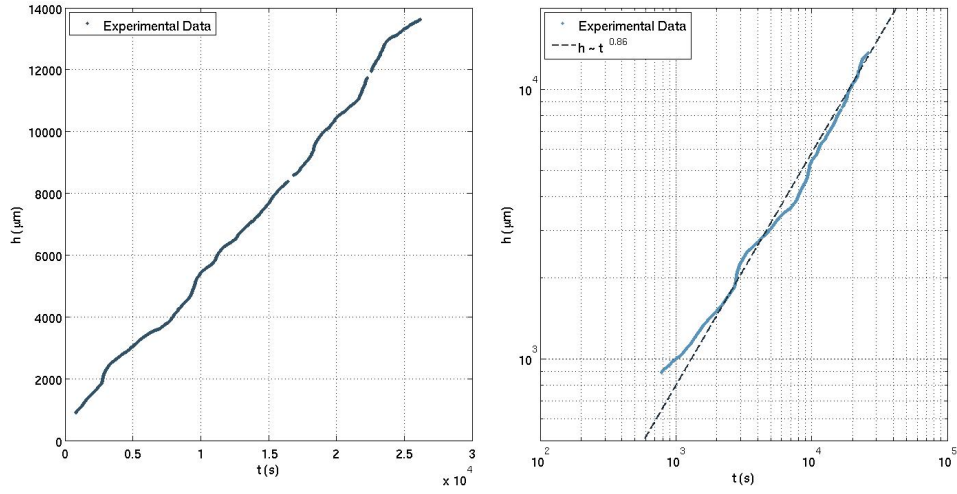

Figure 20: Experimental dynamics of the averaged front position in a hydrophobic microchannel for high driving pressure differences. It is shown in a linear scale (at the left) and a logarithmic scale (at the right)
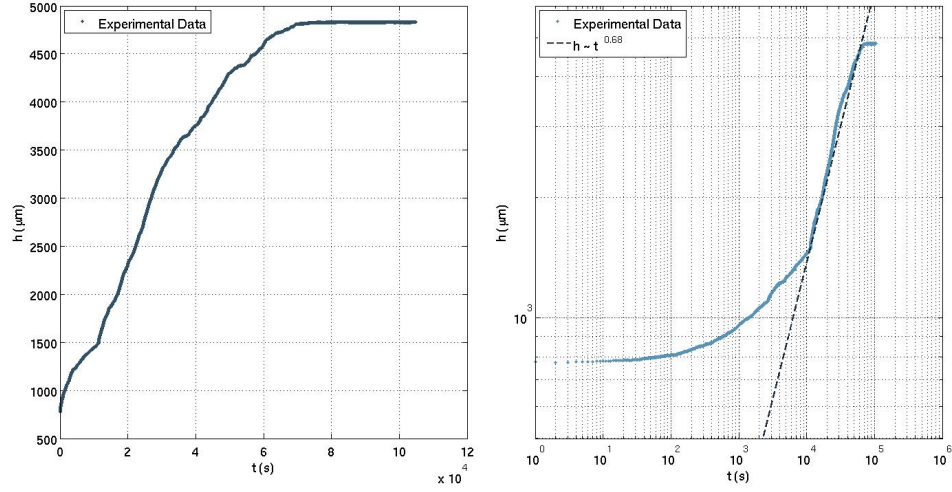
Figure 21: Experimental dynamics of the averaged front position in a hydrophobic microchannel for medium driving pressure differences. It is shown in a linear scale (at the left) and a logarithmic scale (at the right)
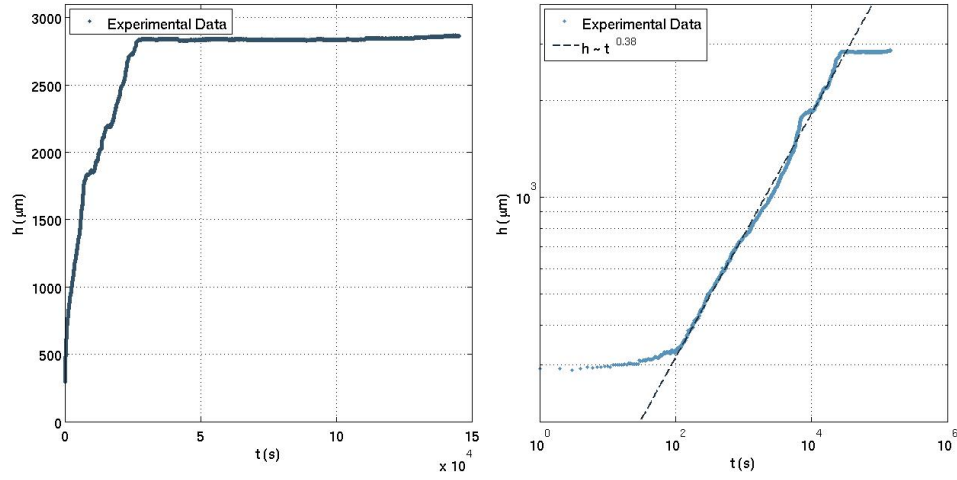

Figure 22: Experimental dynamics of the averaged front position in a hydrophobic microchannel for low driving pressure differences. It is shown in a linear scale (at the left) and a logarithmic scale (at the right)
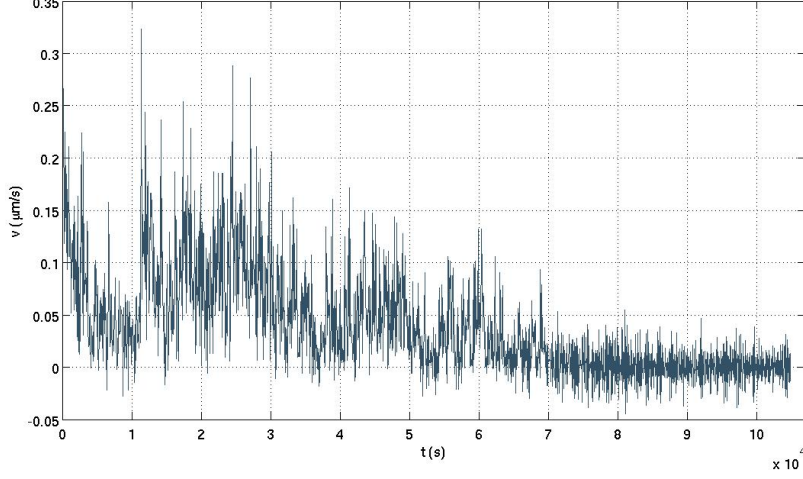
Figure 23: Experimental velocity as a function of time of a fluid front advancing in a hydrophobic microchannel

tained for the exponent ν are different. That is, when the driving pressure difference applied is high, the exponent goes as $\nu = 1$, but when this pressure difference is reduced, the exponent ν also decreases, obtaining an exponent as small as $\nu = 0.38$. In this case, typical Washburn law $h \sim t^{1/2}$ is not accomplished, revealing that new phenomena drive the fluid front along the microchannel.

Pressure in the experiments is lowed so much as the hydrophobicity allows because, if pressure is too much low, front stops and does not travel along the microchannel, but never a coefficient lower than $\nu = 0.38$ is obtained.

From the averaged front position, the numerical derivative is calculated in order to get the dynamics of the velocity. An example is shown in figure 23.

It can be observed the presence of fluctuations in the velocity, having

$$v(t) = v_o(t) + \delta v(t), \tag{30}$$

where $v_o(t) \sim t^{\nu-1}$ is the mean temporal dependency that comes from equation 29. The fluctuating term $\delta v(t)$ is attributed to the pinning effects at the interface induced by the roughness present at the surfaces of the channel. To study the behavior of these fluctuations, their distribution is calculated. In figures 24, 25 and 26 these distributions are shown for three different driving pressure differences.

It is observed that all the distributions are very asymmetric and non-Gaussian distributed. They show a tail for big positive values, which means
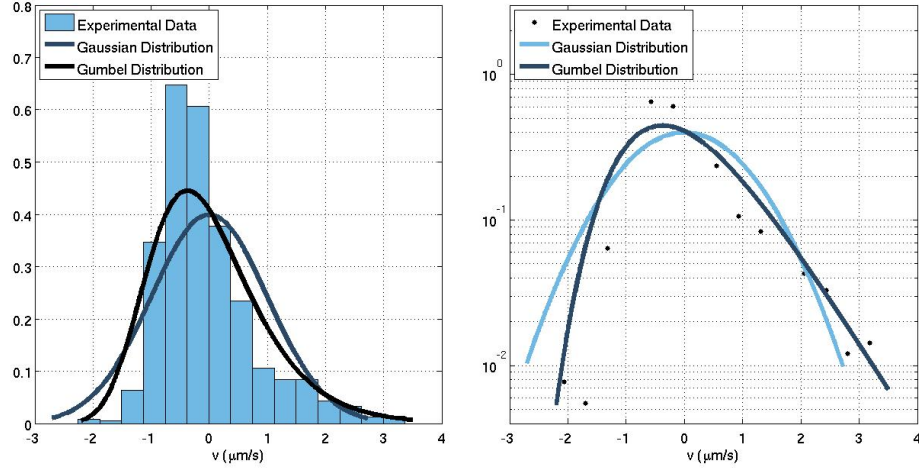
24

Figure 24: Distribution of the experimental fluctuations of the velocity of the fluid front in a hydrophobic microchannel for high driving pressure differences. It is also plotted a Gaussian distribution and a Gumbel distribution, in linear and semilogarithmic scales
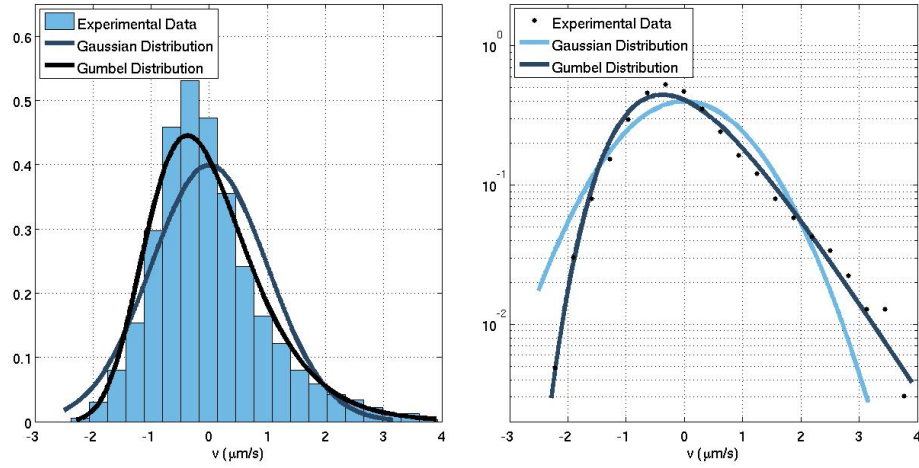

Figure 25: Distribution of the experimental fluctuations of the velocity of the fluid front in a hydrophobic microchannel for medium driving pressure differences. It is also plotted a Gaussian distribution and a Gumbel distribution, in linear and semilogarithmic scales
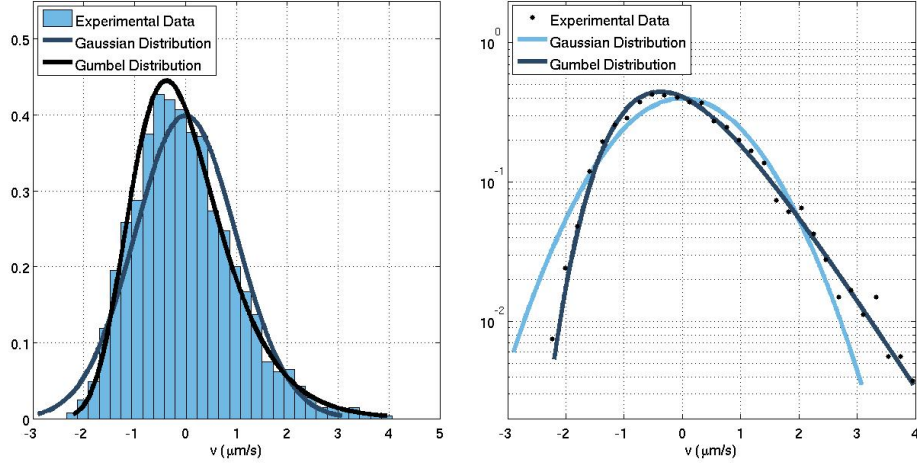
Figure 26: Distribution of the experimental fluctuations of the velocity of the fluid front in a hydrophobic microchannel for low driving pressure differences. It is also plotted a Gaussian distribution and a Gumbel distribution, in linear and semilogarithmic scales

that there is an unusual increase of events of large velocity. These distributions are then given by a Generalized-Gumbel distribution [12]

$$P_a(x) = \frac{a^a b_a}{\Gamma(a)} \exp\left\{ -a\big[b_a\left(x + s_a\right) + \exp\left\{-b_a\left(x + s_a\right)\right\}\big]\right\} ,$$

where x is the variable of study and $\Gamma(a)$ is the Gamma function. There are also three parameters: a, b_a and s_a but only a is free because the other two depend on it, as seen next in their expressions:

$$b_a = \frac{\sqrt{\frac{\mathrm{d}^2 \ln \Gamma(a)}{\mathrm{d}a^2}}}{\sigma_x} \qquad\qquad s_a = <x> + \frac{\ln a - \frac{\mathrm{d}\ln\Gamma(a)}{\mathrm{d}a}}{b_a} ,$$

where $<x>$ and σ_x are mean and variance of x data.

The value of the free parameter, a, is related with the distribution of the fluctuations through the third moment of the statistics analysis, also called skewness:

$$\gamma = \frac{1}{N} \sum_i \left[\frac{v - v_0}{\sigma_v}\right]^3 \tag{31}$$

The skewness is related to how asymmetric is the distribution. That is, when a distribution is very symmetric, it has $\gamma \simeq 0$ and, when it is asymmetric, the skewness takes values different from zero.
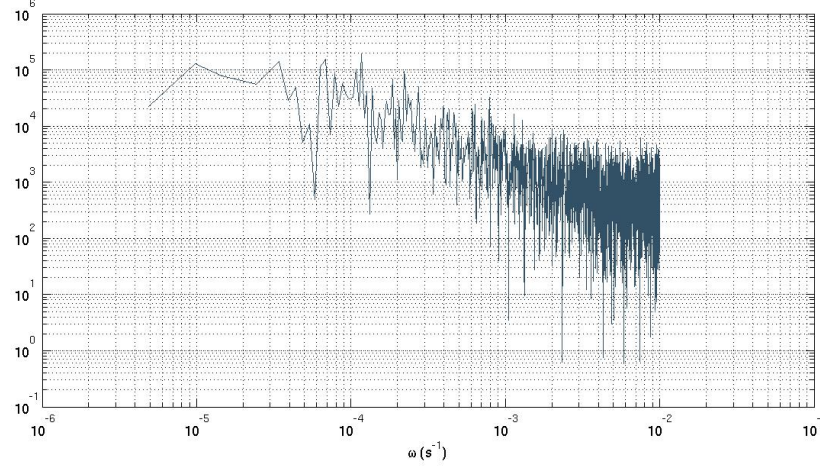
26

Figure 27: Logarithmic representation of the power spectrum of the experimental velocity of a fluid front in a hydrophobic microchannel

The relation between the Gumbel free parameter a and the skewness γ is:

$$\gamma \sim \frac{1}{\sqrt{a}} \tag{32}$$

Generalized Gumbel distribution in figures 24, 25 and 26 is calculated using the values of the free parameter obtained with relation 32. It is observed a very good agreement either for high and low driving pressure differences applied.

Generalized Gumbel distribution has been found in very different research areas like economy, earthquakes risk or quantum physics [13]. Its behavior is a typical signature of a burst like dynamics. This kind of distribution is found in fluid physics associated to phenomena like avalanches [17].

Only when the experiments of hydrophobic microchannels are carried out at very high driving pressure differences, having that roughness of the walls of the microchannel and pinning effects become irrelevant, a Gaussian distribution is obtained from the analysis of the fluctuations of the velocity.

From the velocity profile, it can also be calculated the power spectrum. It has been calculated for the experiments at low driving pressure differences, obtaining the result shown in figure 27. It is observed that the values of the power spectrum increase when the frequency decreases. This reveals the existence of long-range temporal correlations. The power spectrum has also been calculated for the case of experiments at very high driving pressure differences, obtaining the same behavior of figure 19 from the hydrophilic

27

microchannels, which is the expected result since the fluctuations in the velocity are also Gaussian distributed.

5 Conclusions

After all the analysis shown in this work, new results have been obtained.

It is obtained that for hydrophilic microchannels the dynamics of the mean front position follows a power law

$$h \sim t^{\nu}, \tag{33}$$

with an exponent going from $\nu = 1$ for high driving pressure differences to $\nu = 0.5$ for low driving pressure differences, which corresponds to the typical Washburn law. The distribution of velocities follows a Gaussian distribution, having the same behavior than for macroscopic channels.

In the case of hydrophobic microchannels, the dynamics of the averaged front position of the fluid front also follows a power law

$$h \sim t^{\nu}, \tag{34}$$

but with an exponent ν taking as small values as $\nu = 0.38$ when low driving pressure differences are applied. This exponent differs from the $\nu = 0.5$ from typical Washburn law.

The distribution of velocities of a fluid front advancing in hydrophobic microchannel shows long-range temporal correlations and follows a Gumbel distribution that correctly characterizes avalanches.

This result implies that a combination of pinning due to the roughness of the walls of the microchannel and the hydrophobicity affects the dynamics of the fluid front.

When the driving pressure differences are very high, the pinning effect becomes irrelevant, having that the distribution of velocities becomes Gaussian.

Appendix A Methods and Material Fabrication

Microchannels are one of the most important element in the experiment because behavior of the fluid is supposed to depend on how they are fabricated, mainly in the material used and the size they have. Because of that, this is explained in detail in the following sections.

There are two types of microchannels used in the experiments: a first type, made of a hydrophilic material and a second type, made of hydrophobic material. Fabrication of each type is very different because the characteristics of each material force to apply specific methods.

A.1. Fabrication of PMMA microchannels

Polymethyl methacrylate (PMMA) is a polymer used due to its low hydrophobicity properties with purified water. Its fabrication is fast, clean and non-expensive, having a good material to use in the experiments.

To start with the fabrication [18], it is necessary to have some material:

- Oven heating temperatures up to 150°C

- PMMA sheets

- Metal clamp

- Tungsten wire with the diameter of the future chips, typically of 150 μm diameter.

- Araldite 2014 epoxy adhesive glue

First, two PMMA sheets have to be cut with a suitable size, which depends on the size of the microchannel required. Typical size of PMMA sheets for microchannels used in this work is $50\ mm \times 20\ mm$. Then, in one of the pieces two holes of $1\ mm$ diameter have to be drilled. Their position will correspond to both ends of the microchannel.

After that, the tungsten wire has to be put on the drilled PMMA piece. One end of the wire has to match up with the holes, as shown in figure 28. Finally, the blank PMMA piece is placed on top, matching up with the other PMMA piece bellow. It is important to have the tungsten wire well positioned, in such a way that it lines up with the holes. It is better to mount all this directly on the clamp, in order to make the process easier.

When the good configuration is obtained, the clamp can be tightened and placed in the oven. It has to be heated at $140°C$ for 5 minutes. Then, the clamp has to be re-tightened and heated for 10 additional minutes.

Then, the PMMA device can be removed from the clamp, and the tungsten wire pulled out. Finally, some glue can be applied to seal up the open end from where the wire has been removed.
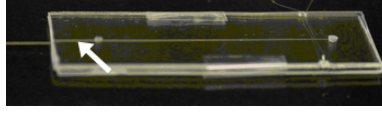
Figure 28: PMMA piece with two holes and the tungsten wire (arrow), from [18]
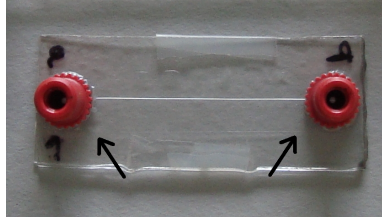

Figure 29: PMMA microchannel with connectors (arrows)

The microchannel has been built. To make its manipulation easier, some connectors can be glued to the two outflows, as shown in figure 29.

PMMA microchannels built up with this technique have cylindrical section with a diameter, which is determined by tungsten wire diameter, not smaller than 100 μm because if tungsten wire has small diameter, then PMMA cannot mix up around it and the microchannel is not built. Therefore, if smaller microchannels need to be used, another technique has to be used. In the case of this work, 150 μm microchannels are small enough to study wall effects and verify washburn law in low hydrophobic microchannels.

In order to study high hydrophobic microchannels, another material is used: PolyDiMethylSiloxane (PDMS), which is a largely used bio-compatible material for microfluidic applications. PDMS microchannels can be built with a different technique, as explained below.

A.2. Fabrication of PDMS microchannels

As said before, for studying what happens if the microchannel is highly hydrophobic, another material has to be used for building up the devices. This material is PDMS, a soft polymer with low affinity to water and proved bio-compatibilities.

For building up a PDMS device, two different methods can be chosen: one is the same than for PMMA chips, and the other is a rapid prototyping method [19]. The first one has been shown in the section above, so now the other will be explained: this technique allows to fabricate microchannels smaller than the ones from PMMA, until 20 μm wide. There is also a big difference between these microchannels and the others: those have cylindrical section, and the new ones have rectangular form. This difference is not

a problem because both have small size, allowing important wall effects.

This technique is also a non-expensive one, but it needs some special equipment and material, which is:

- High resolution laser printer

- Photosensible resin, for example *SU8-50 from MicroChem*, which is a negative photoresist

- Spinner

- High temperature oven

- PDMS pre-polymer and curing agent

The steps of the procedure are:

1. Design a mask and print it on a transparent sheet with high resolution.

2. With SU8 photo resin and the mask designed, fabricate a master.

3. Fabricate the PDMS replica.

Details of the fabrication are in [19]. All the fabrication was made in Parc Científic de Barcelona by specific personal.

Appendix B Programs

B.1. Image analysis

```
for fotos=1:25000 % These are all photographs in the file
    I=imread(fileNames{fotos}); % fileNames is the string
                                % where are located the files.
    Ig=rgb2gray(I);
    J=imread('v01 00001.jpg');
    Jg=rgb2gray(J);

    %Now images are cut:
    Ig2=imcrop(Ig,[11 232 700 30]); % The numbers are:
                                    % [FirstColumn FirstRow
                                    % (columns-1) (rows-1)]
    Ig3=imadjust(Ig2); %This allows to improve contrast.



    % Conversion to a binary image. Threshold value has to
    % be set and depends on the video.
    bn=<=80;

    %Now the binary image is cleaned.
    bnlimpia=imerode(bn,SE);

    %%%%%%%%%%%%%%%%%%%%%%%%%%%%%%%%%%%%%%%%%%%%

    %Here the image is prepared to be analyzed
    label=bwlabel(bnSUPERlimpia,8);
    s=size(bnSUPERlimpia);
    columns=s(2);
    rows=s(1);

    %The front has to occupy all the width of the microchannel; if
    %not, it could be a spot.
    for i=1:columns
        for j=1:columns
            if label(1,i)==label(rows,j) && label(1,i)~=0
                n=label(1,i);
                break
            end
        end
    end
```

32

```
    %Now the position of the front is measured:
    for k=1:rows
            blancos=find(label(k,:)==n);
             M=blancos(end);
             Resultado01filas(k,fotos)=M;
    end

% clear i j k s columns rows n


end

%Mean position is finally obtained.
Resultado01=mean(Resultado01filas);

%Saving the result:
save Resultado01.mat
```

B.2. Calculation of velocity values and distribution

```
load VelocidadHistGumbel.mat
tfin=numel(Espacio45);

for tpaso=40 %Time step is set at the beginning

    LimiteHist=3;
    LimiteHistNeg=-LimiteHist;
    binshist2=30;

    h45_tpaso=[];
    t45_tpaso=[];
    h45_tpaso=Espacio45(1:tpaso:tfin);
    t45_tpaso=Tiempo45(1:tpaso:tfin);

    %%%%%%%%%%%%%%%%%%%%%%%%%%%%%%%%%%%%%%%%%%
    %Derivative: calculation of the velocity
    v45_tpaso=[];
    tderiv45_tpaso=[];
    h=h45_tpaso;
    t=t45_tpaso;

    Derivadah=[];
    ifinal=numel(h)-1;

    for i=1:ifinal
        restah=h(1,i+1)-h(1,i);
        restat=t(1,i+1)-t(1,i);
        cociente=restah/(restat);
        Derivadah=[Derivadah cociente];
    end


    tparaderivadah=t(1,1:ifinal);


     v45_tpaso=Derivadah';
     tderiv45_tpaso=tparaderivadah';

    clear h t a ifinal i restah k cociente
    clear restat h t tparaderivadah Derivadah

    %%%%%%%%%%%%%%%%%%%%%%%%%%%%%%%%%%%%%%%%%%
```

```matlab
    %Fit for normalization of velocity values
    Fit45=fit(tderiv45_tpaso,v45_tpaso,'power1');
    ayyy=Fit45(tderiv45_tpaso);
    V45_tpaso_FEA=(v45_tpaso-ayyy)';
    tderiv45_tpaso_FEA=tderiv45_tpaso';
    tderiv45_tpaso=tderiv45_tpaso';

    %%%%%%%%%%%%%%%%%%%%%%%%%%%%%%%%%%%%%%%%%%
    %Normalization
    V45NORM_tpaso_FEA=(V45_tpaso_FEA-mean(V45_tpaso_FEA))
                                    ./std(V45_tpaso_FEA);

    %%%%%%%%%%%%%%%%%%%%%%%%%%%%%%%%%%%%%%%%%%
    %Removing wrong values in the velocity
    DosSigma=2*std(V45NORM_tpaso_FEA);
    V45NORM_tpaso=V45NORM_tpaso_FEA;
    S=numel(V45NORM_tpaso_FEA);
    LosFeos=find(abs(V45NORM_tpaso_FEA)>LimiteHist);
    LS=numel(LosFeos);
    for i=LS:-1:1
        tatocao=LosFeos(i);
        V45NORM_tpaso(tatocao)=[];
        tderiv45_tpaso(tatocao)=[];
    end

    LosFeos2=find(V45NORM_tpaso<LimiteHistNeg);
    LS2=numel(LosFeos2);
    for i=LS2:-1:1
        tatocao2=LosFeos2(i);
        V45NORM_tpaso(tatocao2)=[];
        tderiv45_tpaso(tatocao2)=[];
    end
    clear S i LosFeos LS tatocao LS2 LosFeos2 tatocao2

    %%%%%%%%%%%%%%%%%%%%%%%%%%%%%%%%%%%%%%%%%%
    %Calculation of the skewness
    Gammatpaso=1/numel(V45NORM_tpaso).*
            sum((V45NORM_tpaso-mean(V45NORM_tpaso))
            .^3./(std(V45NORM_tpaso))^3);
    Gamma(1,tpaso)=Gammatpaso;
    tGamma(1,tpaso)=tpaso;

end
```

```
%%%%%%%%%%%%%%%%%%%%%%%%%%%%%%%%%%%%%%%%%%%%
%Calculation and standardization of the histogram
[AlturaHistV45_EjeAjust BaseHistV45_EjeAjust]=
                                hist(V45NORM_tpaso,binshist2);
sumaV45EjeAjust=sum((AlturaHistV45_EjeAjust.*(max(V45NORM_tpaso)
                                -min(V45NORM_tpaso))./binshist2));
AlturaHistV45_EjeAjust_NORM =AlturaHistV45_EjeAjust
                                ./sumaV45EjeAjust;

clear sumaV45EjeAjust

%%%%%%%%%%%%%%%%%%%%%%%%%%%%%%%%%%%%%%%%%%%%
%Calculation of Gumbel distribution with the specific skewness
%of data
a=1/(Gammatpaso)^2;
sigmax=1;
mediax=0;
ParametroGumbel45_aEjeRecortado=a;

b=sqrt(psi(1,a))/sigmax;

s=mediax+(log(a)-psi(0,a))/b;

K=a^a*b/gamma(a);


Gumbel=K.*(exp(-b.*(x+s)-exp(-b.*(x+s)))).^a;

%%%%%%%%%%%%%%%%%%%%%%%%%%%%%%%%%%%%%%%%%%%%%%
%Calculation of Gaussian distribution:
x=V45NORM_tpaso;
Gausiana=normpdf(x,0,1);

%%%%%%%%%%%%%%%%%%%%%%%%%%%%%%%%%%%%%%%%%%%%%%
%Plotting experimental data, Gumbel and Gaussian distribution
%together

figure
semilogy(BaseHistV45_EjeAjust,AlturaHistV45_EjeAjust_NORM ,
                                '*k','MarkerSize',6)
hold on
semilogy(x,Gumbel,'.','Color',[0.2,0.45,0.61],'MarkerSize',12)
semilogy(x,Gausiana,'.','Color',[0.2,0.45,0.61])
```

```
legend('Experimental Data',['Gumbel Distribution with a=',
                   num2str(ParametroGumbel45_aEjeRecortado),
                   ' calculated from skewness','Gaussian
                   Distribution'])
title(['Normalized Histogram,  Time step ',num2str(tpaso),' sec'])
xlabel('Velocity (\mu m/sec)')
```

B.3. Calculation of the power spectrum

```
load PowerSpectrum.mat

%%Experimental velocity
t=tderiv36_tpaso50segs;
V=V36NORM_tpaso50segs;

%Time step:
tpaso=50;


%%%%%%%%%%%%%%%%%%%%%%%%%%%%%%%%%%%%%%%%%%%%%
%Calculation of the frequency
Fs=1/(t(2)-t(1));
L=numel(V);

%%%%%%%%%%%%%%%%%%%%%%%%%%%%%%%%%%%%%%%%%%%%%
%Fast Fourier Transform Algorithm
NFFT=2^(nextpow2(L));
FT=fft(V,NFFT);
P=(abs(FT(1:NFFT/2))).^2;
w=Fs/2*(linspace(0,1,numel(P)));

%%%%%%%%%%%%%%%%%%%%%%%%%%%%%%%%%%%%%%%%%%%%%%
%Plot
figure
loglog(w,P,'r')
title(['Power Spectrum in logarithmic scale'])
xlabel('Frequency \omega')
ylabel('Power Spectrum')
grid on
```

References

[1] M. Queralt-Martín, Rodríguez-Trujillo, M. Arundell, E. Corvera Poiré, A. Hernández-Machado, *Pinning and avalanches in hydrophobic microchannels*, preprint (2009)

[2] P. Tabeling, *Introduction to microfluidics*, Oxford University Press (2005)

[3] D. J. Beebe *et al.*, *Physics and applications of microfluidics in biology*, Annu. Rev. Biomed. Eng. **4**:262-286 (2002)

[4] G. M. Whitesides, *The origins and the future of microfluidics*, Nature **442**, 368-373 (2006)

[5] D. R. Reyes, *Micro total analysis systems. 1. Introduction, theory and technology*, Anal. Chem., **74**, 2623-2636 (2002)

[6] M. Bravo Gutiérrez, *Dinámica de fluidos viscosos y viscoelásticos en microcanales*, Universidad Nacional Autónoma de México (2007)

[7] T. M. Squires et *et al.*, *Microfluidics: Fluid physics at the nanoliter scale*, Review of Modern Physics, **77**(3), 977-1026 (2005)

[8] L. D. Landau *et al.*, *Fluid mechanics*, Oxford (1959)

[9] M. Pradas, *Interfaces in disordered media. Scaling growth, avalanche dynamics, and microfluidic fronts*, PhD Thesis, Universitat de Barcelona (2009)

[10] C. Chatfield, *The analysis of time series. An introduction*, Chapman and Hall (1991)

[11] H. J. Nussbaumer, *Fast Fourier transform and convolution algorithms*, Springer (1982)

[12] E. J. Gumbel, *Statistics of extremes*, Columbia University Press (1958)

[13] J. Beirlant *et al.*, *Statistics of extremes. Theory and applications*, John Wiley & Sons Ltd (2004)

[14] S. Kotz *et al.*, *Extreme value distributions. Theory and applications*, Imperial College Press (2000)

[15] E. Bertin, *Global fluctuations and Gumbel statistics*, Phys. Rev. Lett. **95**, 17 (2005)

[16] S. T. Bramwell, *The distribution of spatially averaged critical properties*, Nature Phys. **5**, 444-447 (2009)

[17] M. Rost *et al.*, *Fluctuations of fluid invasion into disordered media*, Phys. Rev. Lett. **98**, 5 (2007)

[18] M. Arundell et *et al.*, *Chips & Tips: Rapid prototyping of a PMMA microfluidic chip with integrated platinum electrodes*, Chips and Tips, Lab on a Chip, **8**(11), (2008)

[19] R. Rodríguez-Trujillo , *High speed microfluidic devices for particle counting on a chip*, PhD Thesis, Universitat de Barcelona (2008)